OPEN ACCESS
IOP Publishing
Measurement Science and Technology
Meas. Sci. Technol. **31** (2020) 045014 (14pp)
https://doi.org/10.1088/1361-6501/ab5e98

Nine-hundred-channel single-shot surface roughness measurement using hyperspectral interferometry

Tobias V Reichold, Pablo D Ruiz and Jonathan M Huntley

Wolfson School of Mechanical, Electrical and Manufacturing Engineering, Loughborough University, Loughborough LE11 3TU, United Kingdom

E-mail: P.D.Ruiz@lboro.ac.uk and T.Reichold@lboro.ac.uk

Received 26 June 2019, revised 3 December 2019
Accepted for publication 4 December 2019
Published 14 January 2020

Abstract

A recently developed hyperspectral interferometer has been applied, for the first time, to the single-shot measurement of surface roughness. Traditional optical surface profiling techniques, such as coherence scanning interferometry (CSI) or focus variation microscopy, require long scan times and mechanical motion of the imaging objectives, making them vulnerable to environmental disturbances and thus inappropriate as an embedded metrology tool for production. Hyperspectral interferometry (HSI) answers these problems by capturing spatial and spectral information to reconstruct the surface profile, from 900 locations measured in parallel, in a single shot. We report here measurement results with both HSI and CSI from 12 individual roughness samples taken from Rubert roughness gauges covering the roughness range $R_a = 0.025 - 50\,\mu\text{m}$. Very good agreement was obtained for S_a values in the range 3–30 μm, where the HSI S_a values were mostly within a few per cent of (and at worst 24% away from) those measured by CSI S_a. An alternative measure of roughness, based on averaging the widths of the Fourier transform peak of the individual HSI interference signals, is shown to be a statistically reliable measure of local roughness in the medium to high roughness regime, i.e. for S_a values of 0.8 μm and above. The results thus demonstrate the technique's potential for real-time surface quality inspection in manufacturing.

Keywords: metrological instrumentation, interferometric imaging, surface measurements, local surface roughness, pinhole array, hyperspectral, single-shot

(Some figures may appear in colour only in the online journal)

1. Introduction

Metrology tools can play an important role in enabling the widespread adoption of new manufacturing technologies. An example is additive manufacturing (AM) which has grown significantly in popularity in recent years, thanks to its ability to manufacture components with complex geometries over a wide range of length scales. The geometries may include internal features such as hollow cavities, composition gradients and microstructures which would be impossible to manufacture by traditional subtractive manufacturing (SM) techniques [1, 2]. Furthermore, as AM is becoming more mainstream the cost of the manufacturing process decreases, thus improving its commercial viability [3, 4]. Metallic printing techniques such as selective laser melting (SLM), formally known as laser powder bed fusion in ISO terms, electron beam melting (EBM) and direct metal laser sintering (DMLS) are commonly used for heavy duty applications. To emphasise how heavy-duty AM parts can be, in 2013 SpaceX was able to successfully 3D print the engine chamber for the SuperDraco thrusters using DMLS entirely in-house. Each thruster can provide up to 71 kN of thrust and eight of them will power the SpaceX Dragon 2 crew capsule [5, 6].

Irrespective of the printing method, some of the main concerns of the finished component in AM are the surface roughness, and the repeatability of the final dimensions, as these have a direct impact on the function of the component. For example, printing an even, smooth surface is challenging due to the inherent layering of the printing material [1, 3, 7]. The utilized material, particle size and distribution, layer thickness, step over and local surface slope have a direct impact on the surface roughness in addition to formation of defects in the core of the structure [1, 3]. Depending on the use of the component, surface roughness parameters such as arithmetical mean height S_a, root mean square height S_q and equivalent line profile roughness parameters arithmetical mean height R_a and root mean square deviation R_q are typically evaluated by offline inspection instruments in a metrology laboratory.

Two industry-standard non-contact inspection techniques are coherence scanning interferometry (CSI) [8] and focus variation microscopy (FV) [9]. CSI is based on a microscope that uses an interference objective, for example of the Mirau type, producing a reference and object beam with the zero optical path difference (OPD) at a plane in front of the objective. The surface axial position is located by mechanically scanning the objective and finding the maximum of the fringe modulation envelope on a pixelwise basis. A typical field of view (FOV) for CSI at low magnification is of order $1 \times 1\,\mathrm{mm}^2$. The axial scanning speed is usually under $150\,\mu\mathrm{m\,s}^{-1}$ which means that it is only suitable for offline parts inspection as a single axial scan might take several seconds or tens of seconds. In focus variation microscopy, the object or microscope head is moved along the optical axis, in a similar motion path and speed to CSI, and using a conventional microscope objective focus variations are evaluated [1]. All depth slices of a full axial sweep are stacked together to form a 3D height map of the measured object [1, 8]. The scanning speeds and FOV are similar to those for CSI, making focus variation also unsuitable for online surface inspection. Despite the fact that CSI and FV can be optimised for rough surface measurement by controlling system parameters such as magnification, type of illumination, vertical and lateral resolution, signal oversampling and high dynamic range lighting levels, the required mechanical scanning still remains a core limitation [10, 11].

Recent developments in metrology for AM are moving towards *in situ* process analysis to capture potential material defects, surface roughness/quality and monitor laser-generated melt pool size, shape and intensity during printing, rather than in post printing analysis [1, 12]. This is achieved in a variety of ways by implementing normal- or high-speed camera monitoring, single and multiwavelength pyrometers, 1D photodetectors or a combination of these to allow adjustment of the printing parameters on-the-fly [12]. A good example is coaxial sensing, in which the infrared (IR) melting laser in combination with dichroic and beam splitters is used to observe the radiation emitted from the melting pool [1, 13]. This allows determination of the melting pool's temperature distribution and geometry, though not spatial surface data [13]. Another optical surface roughness measurement technique includes laser coherent scattering for in-line surface roughness inspection as found in the QISAB CWS 640 [14]. This is capable of capturing up to a $4 \times 4\,\mathrm{mm}^2$ FOV down to sub-μm lateral resolution with ~1 ms acquisition time [14]. The measurable roughness values are however limited to the range $10\,\mathrm{nm} \leqslant S_q \leqslant 350\,\mathrm{nm}$. This is insufficient to measure, for example, additively manufactured parts for which surface roughness can easily exceed several μm.

A new dimensional measurement technique called hyperspectral Interferometry (HSI) has been developed in recent years. Like CSI, it is based on interferometry with a broadband source, and provides areal coverage of the sample. The current system provides up to 1300 μm depth range and 0.49 μm depth resolution over a FOV $12.5 \times 12.5\,\mathrm{mm}^2$ [1, 15–17]. Compared to CSI and focus variation microscopy, HSI has a reduced number of sample points, although the latest system now provides up to 2500 depth-sensing channels working in parallel [18]. The main benefit compared to CSI and depth from focus systems is that it makes the measurement in a single shot, thus dispensing with all mechanical scanning, and thereby opening opportunities for in-process dimensional metrology.

Recent HSI papers have focussed on optically smooth surfaces. There is considerable potential benefit, unrealised so far, if HSI could be extended to provide single shot areal characterisation of optically rough surfaces produced, for example, by AM. ISO roughness measurement standards (ISO 25178-1:2016) specify recommended procedures for instruments such as CSI and FV. However, they cannot be applied straightforwardly to a hyperspectral interferometer, because CSI and FV sample the height distribution of the surface microstructure with very fine (typically sub-μm) lateral resolution. HSI on the other hand has gaps between the spatial sampling points, within which the spectral data is interlaced, and approximately two orders of magnitude increase in FOV, both of which increase the lateral sampling distance significantly in comparison to CSI or FV. It is therefore of interest to compare alternative approaches which can avoid the need to measure many closely spaced height values. Ideally, each channel of the depth sensor should provide an independent roughness value, to optimise spatial resolution in the sampled roughness field.

In the current paper we investigate the effect of rough surfaces on the signals from a hyperspectral interferometer. In standard HSI analysis, the 1D interferogram from a given channel is Fourier transformed and the location of the principal peak provides the depth value for the region of the sample contributing light to that channel. It is shown here experimentally that surface roughness manifests itself in a broadening of the Fourier peak, thus providing an alternative roughness characterisation parameter to that provided by ISO and other standards. The investigation is made using a set of 12 roughness gauges covering R_a values from 0.025 to 50 μm, as determined independently by CSI and ISO-compliant post-processing algorithms, in order to assess the roughness regimes that are suitable for measurement by HSI.

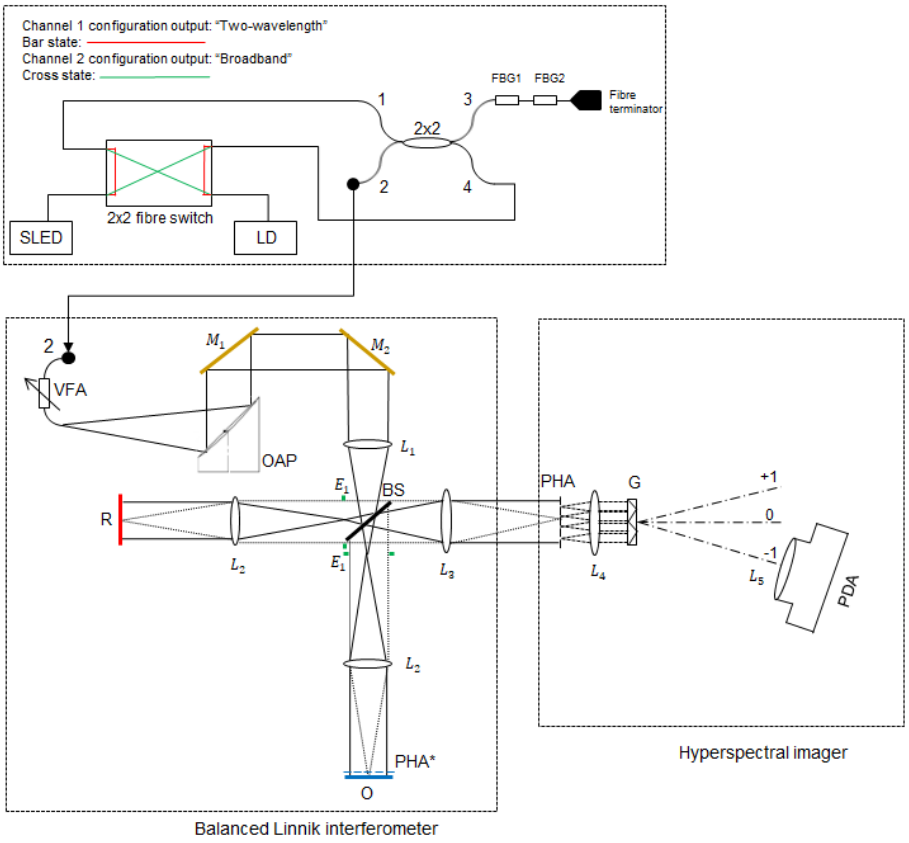

Figure 1. Optical setup, showing: SLD: super-luminescent light emitting diode; FBG_1, FBG_2: fibre Bragg gratings; VFA: variable fibre attenuator; OAP: off-axis parabolic mirror; M_1, M_2: gold steering mirrors; L_1: focusing lens (focal length 135 mm, aperture ratio *f*/6.56); BS: beam splitter; O: object; R: reference mirror; L_2, L_3: achromatic lenses (focal length 135 mm, *f*/6.56); L_4: lens (focal length 135 mm, *f*/2.4); L_5: zoom lens (focal length 70–300 mm, *f*/4–5.6); E_1: aperture stop; PHA: pinhole array; G: diffraction grating 300 lines mm^{-1}; and PDA: photodetector array. PHA* is the image of PHA formed by L_2 and L_3; the positions of the pinholes in this image define the sampling locations for roughness measurement on O.

2. Experimental

2.1. Optical system

The optical system has been described previously in [1, 15, 19], and can be considered an advance (in terms of number of channels and upper bound on surface slope) on the microlens array system presented in [15]. It combines a broadband source, a Linnik interferometer, and an imaging spectrometer similar to that originally developed for astronomy applications [19, 20], as shown in figure 1. One difference between the system used in the current paper and that described in [18] is that the pinhole array size has been reduced from 50 × 50 to 30 × 30 in order to allow more pixels for each spectrum, and to reduce crosstalk between channels.

At the top of the Linnik interferometer box, two alternative input illumination configurations ('Two wavelengths' and 'Broadband') are shown. Light from one of the two illumination configurations enters the Linnik Interferometer at the point labelled 2. The two-wavelength configuration provides two bright circular intensity peaks from each pinhole at known wavelengths λ_1 and λ_2. These act as reference spots during calibration of the instrument. This is achieved by two fibre Bragg gratings (FBG) in series where $\lambda_1 = 820$ nm and $\lambda_2 = 853$ nm with a narrow spectral band <0.01 nm. The FBGs act as wavelength filters allowing only two wavelengths to pass into the system. Rather than producing a continuous line spectrum, they form two points (or spots) in the image plane of the camera. The calibration of the wavenumber axis for each pinhole is described in [15]. The broadband illumination configuration is used for normal measurements. The object is imaged at 1:1 magnification onto an array of pinholes, PHA, where the object wave is mixed with the light from a reference mirror. The imaging in the interferometer is accomplished with a 4*f* system with one focal length separation between each element. The light passing through each pinhole in PHA acts as a quasi-point-source input to the spectrometer, where it is dispersed by a grating so as to produce a 1D interference signal $I(k)$, where k denotes wavenumber. This is imaged onto a high-resolution photodiode array (PDA). The pinhole array provides gaps between spatial sample points with a pitch of 370 μm and 5 μm pinhole diameter within which the spectral information can fall, which is key to the single shot operation of the system. However, it also has the disadvantage that it increases the separation

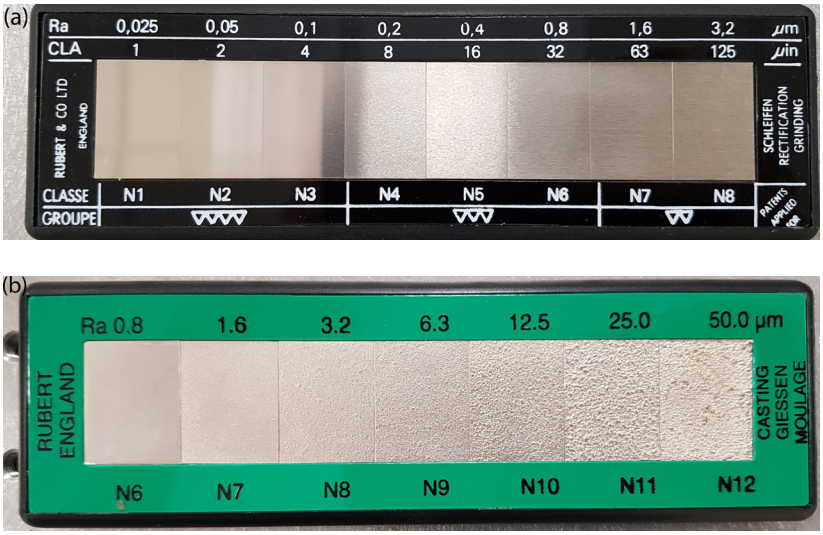

Figure 2. Rubert roughness gauges (a) ground, arithmetic mean roughness range $0.025 \leqslant R_a \leqslant 3.2\,\mu\text{m}$; (b) cast, $0.8 \leqslant R_a \leqslant 50\,\mu\text{m}$.

between neighbouring sample points on the object surface. For the current pinhole array the effective number of useable channels is a 30×30 square grid, delivering a FOV of $11 \times 11\,\text{mm}^2$ with an unambiguous depth range of 1300 µm. All HSI surface maps shown throughout the paper have these dimensions. Each spectrum is sampled by 407 pixels horizontally and is ~6 pixels wide. It should also be noted that due to the small pinhole diameter and low power of the light source, the optimal exposure times are typically in the order of several seconds or more, depending on surface roughness and reflectivity. Calculation times using non-optimized MATLAB GPU code are approximately 30 s for all 900 channels on a HP Z620 with a Nvidia Titan V.

2.2. Samples

The samples under investigation were two Rupert roughness gauges: one ground type from index N1–5 and the other cast type from index N6–12, as shown in figure 2. Each gauge was measured, using a Polytec TMS-500 PRO large FOV CSI, to obtain reference surface roughness values including height and spatial parameters. These include arithmetic mean and root-mean-square height S_a and S_q; autocorrelation length S_{al}; and texture-aspect ratio S_{tr}.

The surface data were processed to extract the surface roughness parameters as follows.

1. The measured surface was levelled using the least squares method to remove global surface slope.
2. Deviations from planar form were removed by subtracting a 2nd order polynomial fit from the levelled data.
3. The waviness and roughness were separated by using a robust Gaussian filter with a cut-off wavelength $\lambda_c = 0.8\,\text{mm}$ for N6 and $\lambda_c = 8\,\text{mm}$ for N10 according to DIN EN ISO 4288:1998 and DIN EN ISO 3274:1998.

The resultant parameter tables for the N6 and N10 indices which are used in later sections are shown in tables 1 and 2.

Table 1. Measured parameters for N6 roughness index.

N6 Parameter table—roughness (robust Gaussian filter, 0.800 mm)				
ISO 25178				
Height parameters				
Sq	0.838	µm		Root-mean-square height
Ssk	0.387			Skewness
Sku	15.4			Kurtosis
Sp	47.1	µm		Maximum peak height
Sv	10.3	µm		Maximum pit height
Sz	57.3	µm		Maximum height
Sa	0.647	µm		Arithmetic mean height
Spatial parameters				
Sal	0.0838	mm	$s = 0.2$	Autocorrelation length
Str	0.824		$s = 0.2$	Texture-aspect ratio
Std	163	°	Reference angle = 0°	Texture ratio

3. Measurement theory

Each pinhole accepts light from a small region on the sample surface. The intensity signal produced when this object wave interferes with the reference wave, and is then dispersed along the wavenumber axis by the spectrometer, can be written

$$I(x_m, y_n, k) = \{I_0(x_m, y_n, k) + I_1(x_m, y_n, k)\cos[kz(x_m, y_n) + \varphi]\} \quad (1)$$

where I_0 and I_1 are intensity values related to the intensity of the object and reference waves; k is the wavenumber ($k = 2\pi/\lambda$); x_m, y_n are the in-plane Cartesian coordinates of the point on the sample surface at the centre of the PSF for the pinhole with indices (m,n), where m and n both run from

Table 2. Measured parameters for N10 roughness index.

N10 parameter table—roughness (robust Gaussian filter, 8.000 mm)				
Height parameters				
Sq	17.2	μm		Root-mean-square height
Ssk	−0.344			Skewness
Sku	5.09			Kurtosis
Sp	249	μm		Maximum peak height
Sv	439	μm		Maximum pit height
Sz	688	μm		Maximum height
Sa	13.5	μm		Arithmetic mean height
Spatial parameters				
Sal	0.344	mm	$s = 0.2$	Autocorrelation length
Str	0.893		$s = 0.2$	Texture-aspect ratio
Std	76.7	°	Reference angle = 0°	Texture ratio

1 to 30 in the current sensor; z is the OPD between object and reference waves; and φ is a phase offset due for example to a complex reflection coefficient.

For an instrument viewing the sample in reflection and on axis, $z = 2h$, where the refractive index of air is taken as 1, h is the distance between the zero-OPD surface—the surface lying in front of the objective lens where object waves and reference wave path lengths are matched—and the point on the sample which is imaged onto the pinhole in question. The spectral envelope $I_1(k)$, where we drop the x_m, y_n dependence to simplify notation, is therefore modulated by a cosinusoidal signal, the frequency of which is proportional to h. $I_0(k)$ is normally subtracted from $I(k)$ before further processing; the Fourier transform of $I(k)$ then consists of a single positive frequency peak. The location of the peak is a direct measure of the distance of the scattering point from the zero-OPD surface, which acts as a close-to-perfectly planar datum, provided the mirrors and lenses are sufficiently well corrected and aligned.

To illustrate the signal processing steps and the effect of surface roughness on the measured signals we consider three scenarios: firstly, a traditional idealised flat surface, secondly a smooth surface but with significant waviness, and finally a rough surface.

3.1. Case 1: ideal flat surface

Consider an ideal flat surface perpendicular to the beam direction as shown in figure 3. The red dashed line represents a cross section through the surface on which object and reference waves have zero optical path difference (‘zero OPD surface’). The three vertical arrowed lines indicate the spatial extent of the region contributing object wave that passes through each of three neighbouring pinholes on the pinhole array. The diameter of each region, d, corresponds to the diameter of the imaging system’s point spread function (PSF),

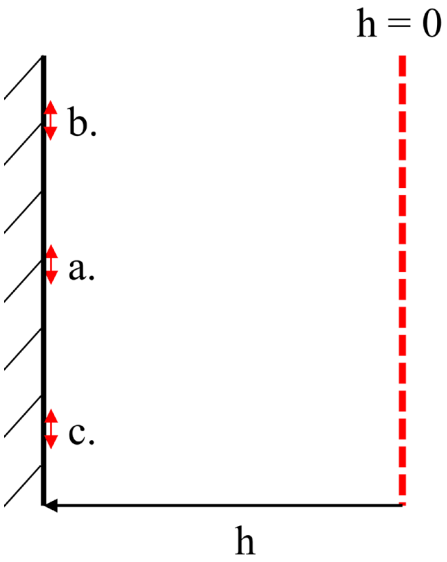

Figure 3. Ideal smooth surface at a distance h from the zero OPD surface. (a)–(c) denotes three independently measured surface regions, each region corresponding to one pinhole.

convolved with the aperture function for a single pinhole, and is ~17 μm for the system described here.

Figure 4 shows three schematic examples of $I(k)$, one for each measurement channel at a fixed distance from the zero OPD surface [19]. All the signals in this figure, and the corresponding figures for the other two cases, are simulated spectra, after removal of the I_0 term to suppress the dc peak. For this case, the Fourier transform peak width is only limited by the spectral bandwidth Δk of the laser source and any windowing performed on the interference signal $I(k)$ as can be seen from equations (9) and (10) in [16]:

$$\delta z' = \gamma \delta z \quad \text{where} \quad \delta z = \frac{2\pi}{N_k \delta k} \tag{2}$$

where $\delta z'$ is the distance between the points on either side of the spectral peak where the amplitude first drops to zero, δz is the separation between sample points in the OPD domain between successive pixels, N_k is the number of sample points in pixels, δk the increment between sample points in the wavenumber domain between successive pixels, and γ takes the value 2 for a rectangular window and 4 for a Hanning window [16].

The Fourier transforms are shown superimposed on the same axes in figure 4 (lower two plots). The non-dimensional frequency on the horizontal axis of the middle plot refers to the total number of cycles within the spectral bandwidth measured by the sensor. This is converted to absolute distance (lower plot) by the calibration with the FBGs. All three peak locations are essentially identical, and hence lie on top of one another, as the three corresponding distances from the zero-OPD surface to the sample surface regions a–c are the same.

3.2. Case 2: real-world wavy surface

Next let us consider a real-world surface that is locally smooth, but has significant waviness, as shown in figure 5. The areal

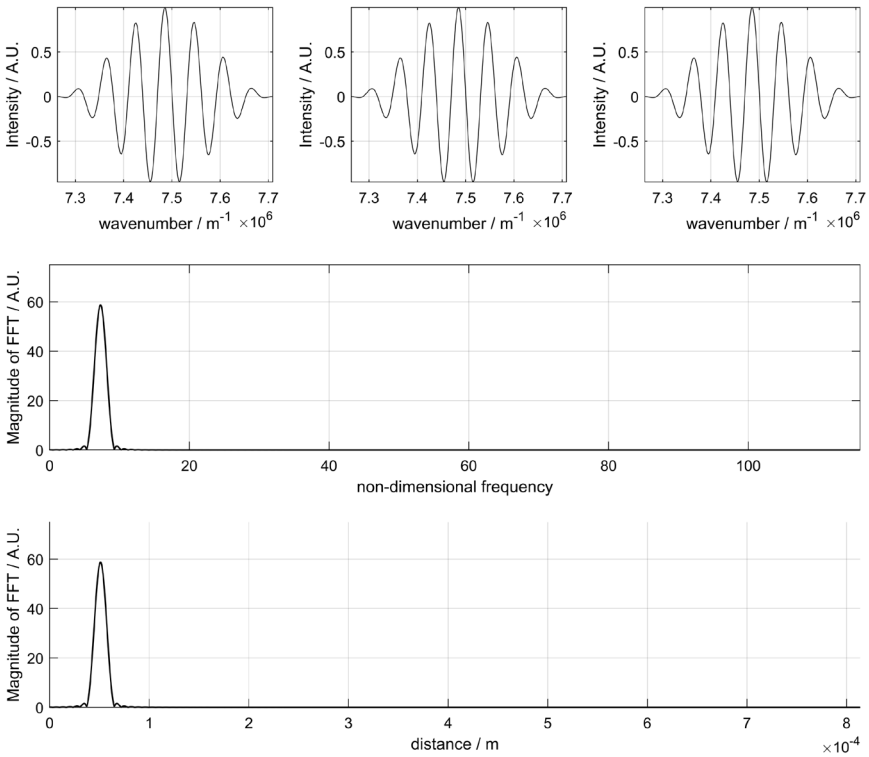

Figure 4. Spectral interference profiles for three points from an ideal flat surface. Top: Intensity of each interference signal. Middle: Fourier transforms of interference signals, superimposed on the same axes, from which the peak positions are evaluated. Bottom: Same as middle but after scaling frequencies to distances.

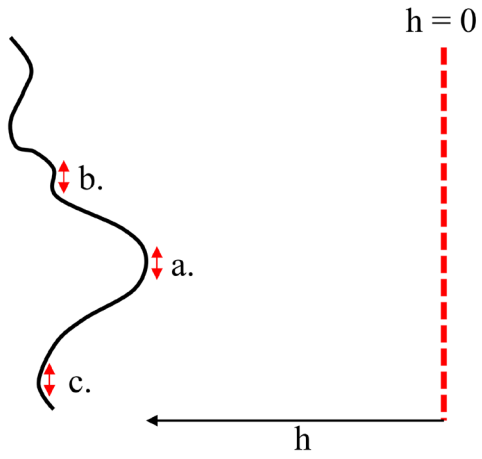

Figure 5. Measurement of a wavy surface. As in figures 3(a)–(c) denote three independently measured surface regions, but these now each have a different distance from the zero-OPD surface (red dashed line).

auto-correlation parameter S_{al} is much greater than the PSF diameter, and the surface height variations within the PSF may thus be neglected. In this case, each channel behaves in the same way as the three channels in case 1, but the waviness results in a different peak location for each.

Figure 6 shows three examples of $I(k)$, one for each measurement channel at a fixed distance from the zero optical path length difference OPD [19]. It can be seen that each interference signal still consists only of a single frequency and corresponding single peak in the Fourier transform. However, the peak locations vary due to the variation of sample distance from the zero OPD surface. If the PSF encompasses a region of the surface with significant slope (e.g. between (a) and (c) in figure 5) then the signal amplitude will in general be reduced and may disappear completely if the slope exceeds a threshold value for the sensor (33 mrad for the HSI system used in this paper [18]).

3.3. Case 3: rough surface

Finally let us consider a rough surface such as a cast Rubert roughness gauge perpendicular to the beam direction. In this case the areal autocorrelation parameter S_{al} may be assumed to be much smaller than the diameter d of the PSF, as shown in figure 7.

In cases 1 and 2 above, each channel gives rise to a single bandwidth-limited peak, due to the (approximately) single depth value of the scattering points within the PSF of the imaging system. For case 3, on the other hand, the PSF may cover multiple surface asperities covering a wide range of depths. This results in the superposition of a range of frequencies in the wavenumber domain, causing distortions to the spectral envelope, and apparent frequency modulation within the envelope. The total peak width in the OPD domain is, as a result, increased, as shown in figure 8.

If a suitable measure of the peak width can be defined, such a parameter would offer the interesting possibility of estimating roughness using the signal from just a single channel. The location of the centre of the peak would provide the mean height value for the sample corresponding to that channel. The system as a whole could then allow spatially resolved surface roughness fields, and height maps, to

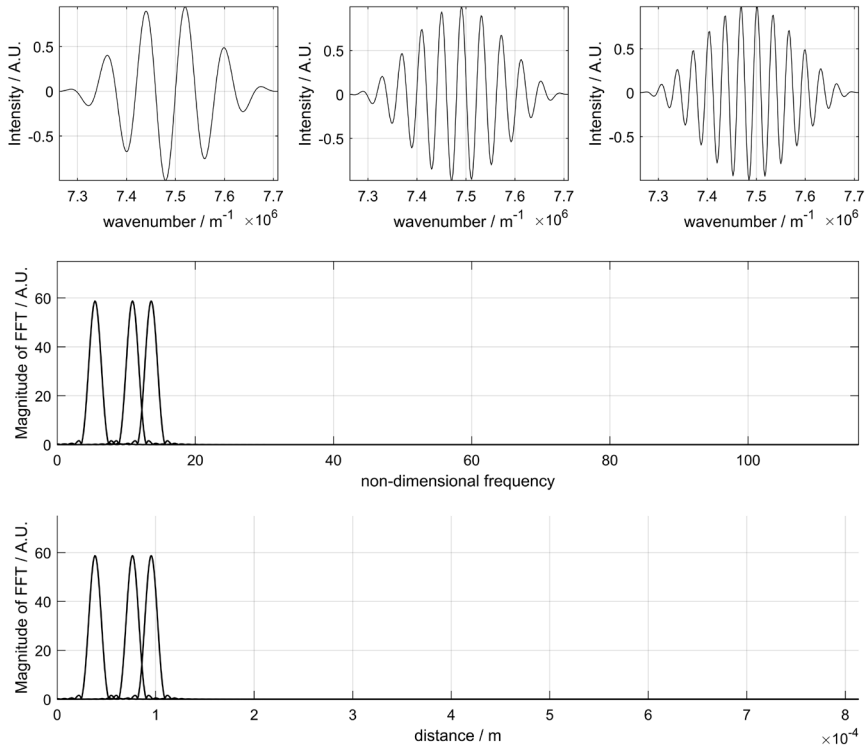

Figure 6. Spectral interference profiles for three channels when measuring a wavy surface. Top: Intensity of each interference signal. Middle: Fourier transform of interference signals, superimposed on the same axes, from which the peak positions are evaluated. Bottom: Same as middle but after scaling frequencies to distances.

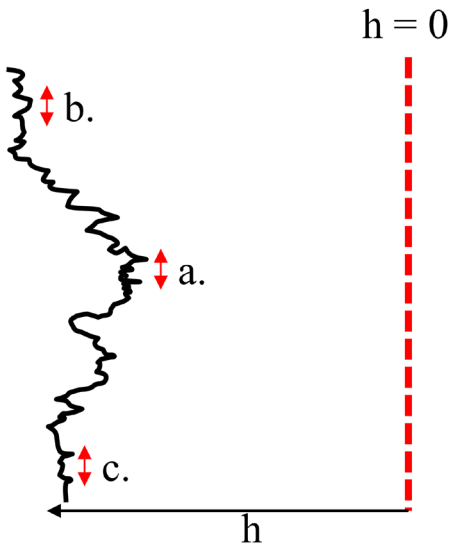

Figure 7. Rough surface at a distance h from the zero-delay line. (a)–(c) denote three independently measured surface points with a diameter equal to the PSF of L_2.

be measured in a single shot. This hypothesis is tested in the next section through a set of experiments on well characterised roughness gauges.

4. Results

The system was tested with the ground and cast Rubert roughness gauges shown in figure 2. Roughness gauge indices N1–5 from the ground gauge and N6–12 from the cast gauge were measured, which provided roughness values spanning the range $R_a = 0.025\,\mu\text{m}$ to $50\,\mu\text{m}$. Each gauge was placed into a kinematic tip/tilt stage to allow angular adjustment of the gauge's frame until approximately perpendicular to the incident beam, and at a fixed distance h from the zero-OPD surface, as shown in figure 9.

The gauge was moved laterally after each individual block had been measured, whilst keeping the front plane of the gauge at approximately the same distance relative to the zero-OPD surface. It should be noted that the individual roughness gauges have independent tilts relative to the frame, which result in a small tilt angle on the subsequent surface measurements.

The 1D interference signal for each measurement channel, $I(k)$, was extracted from the recorded interference spectra image and Fourier transformed. A 1D Gaussian function $g\,(h)$ was fitted to the transform, where g is defined by

$$g\,(h) = A + B\exp\left(-(h - h_c)^2/2\sigma_h^2\right) \tag{3}$$

A, B, σ_h, and h_c are free parameters for a given channel, the values of which are estimated by least squares analysis, and h is the height variable. h_c is the centre of the Gaussian and represents the mean height of the region of the sample lying within the PSF for this channel. σ_h is the standard deviation of the Gaussian peak and is thus the parameter that—we have hypothesised—may provide a 'per channel' estimate of surface roughness. The Gaussian in equation (3) was chosen as the fitting function as it is in common use to describe probability density functions for rough surfaces. Although it may not necessarily be the best fitting function for the Fourier peak

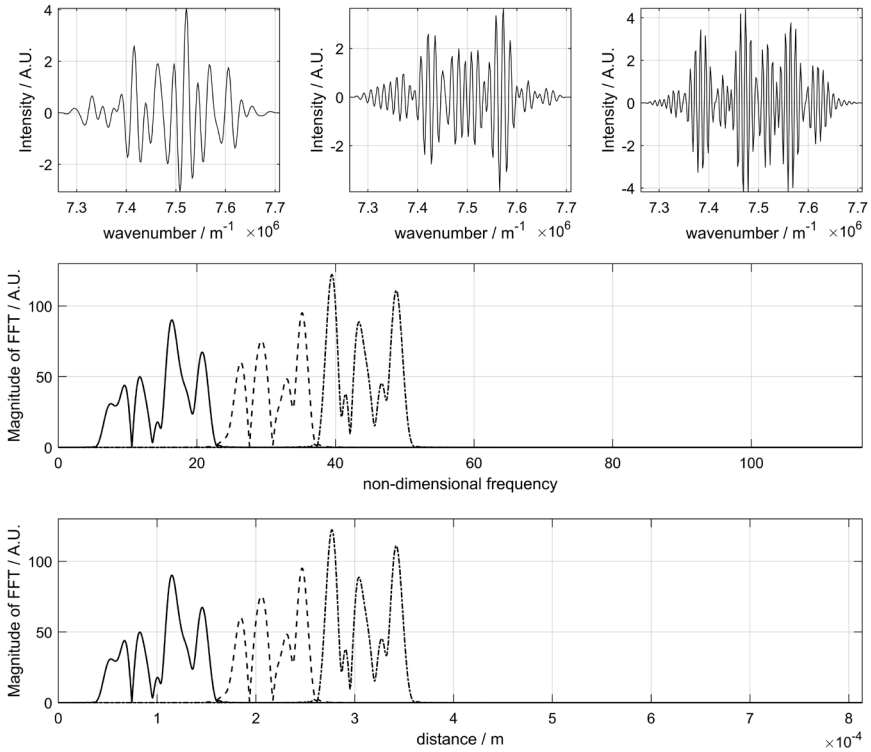

Figure 8. Spectral interferograms for three channels when a rough surface is measured. Top: Intensity of each interference signal. Middle: Fourier transform of interference signals. Bottom: Same as middle but after scaling frequencies to distances.

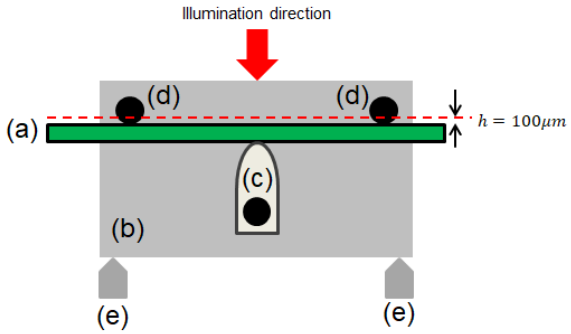

Figure 9. Top view of sample setup for gauges: (a) Rubert roughness gauge, (b) tip/tilt kinematic stage, (c) locking arm, (d) supporting sample rods, (e) fine pitch tilt adjustment screws. Red dashed line: Cross section through zero-OPD surface (not to scale).

shape under certain regimes, it nevertheless provides a useful characterisation across all the roughness scales considered here.

Examples of the spectra from a small subset of all the available measurement channels, for two different roughness values, each with their corresponding surface profile and reference surface measurements, are given in figures 10–15. It is clear that the spectra (figures 10 and 13) are significantly noisier than those previously published for measurements on smooth surfaces [15, 16]. The rough surface creates a random speckle pattern in the scattered light throughout the volume in front of the sample. Whenever a dark speckle happens to fall on a particular pinhole, the resulting spectra therefore have low signal levels (e.g. pupils 547 and 727 in figure 13). The reconstructed surface profiles (figures 11 and 14) given by the spatial distribution of the h_c parameter may be used to calculate a single S_a value for the full field. Note the surface maps shown in figures 11, 12, 14 and 15 are de-tilted only (i.e. deviations from planar form have not yet been removed) to show the similarities in the measured surface shape between HSI and CSI. The S_a values obtained in this way are summarised in table 3 for all the roughness gauges studied and plotted in figure 16 against the S_a value as measured by CSI. The agreement with the CSI data is seen to be very good for gauges N7–N11. For the lower roughness gauges the agreement is poor, though the data still shows a gradual increase in HSI Sa with increasing CSI Sa. The reasons for this are discussed in section 4.

The σ_h values fluctuate from channel to channel, due to the varying depth range of the scattering points within each measurement cell. The average of these values over all the channels with valid data, for a single measurement of a given roughness gauge, will be denoted $\overline{\sigma}_h$. The standard deviation in σ_h, calculated after excluding the channels with erroneous data, is denoted σ_{σ_h}. The

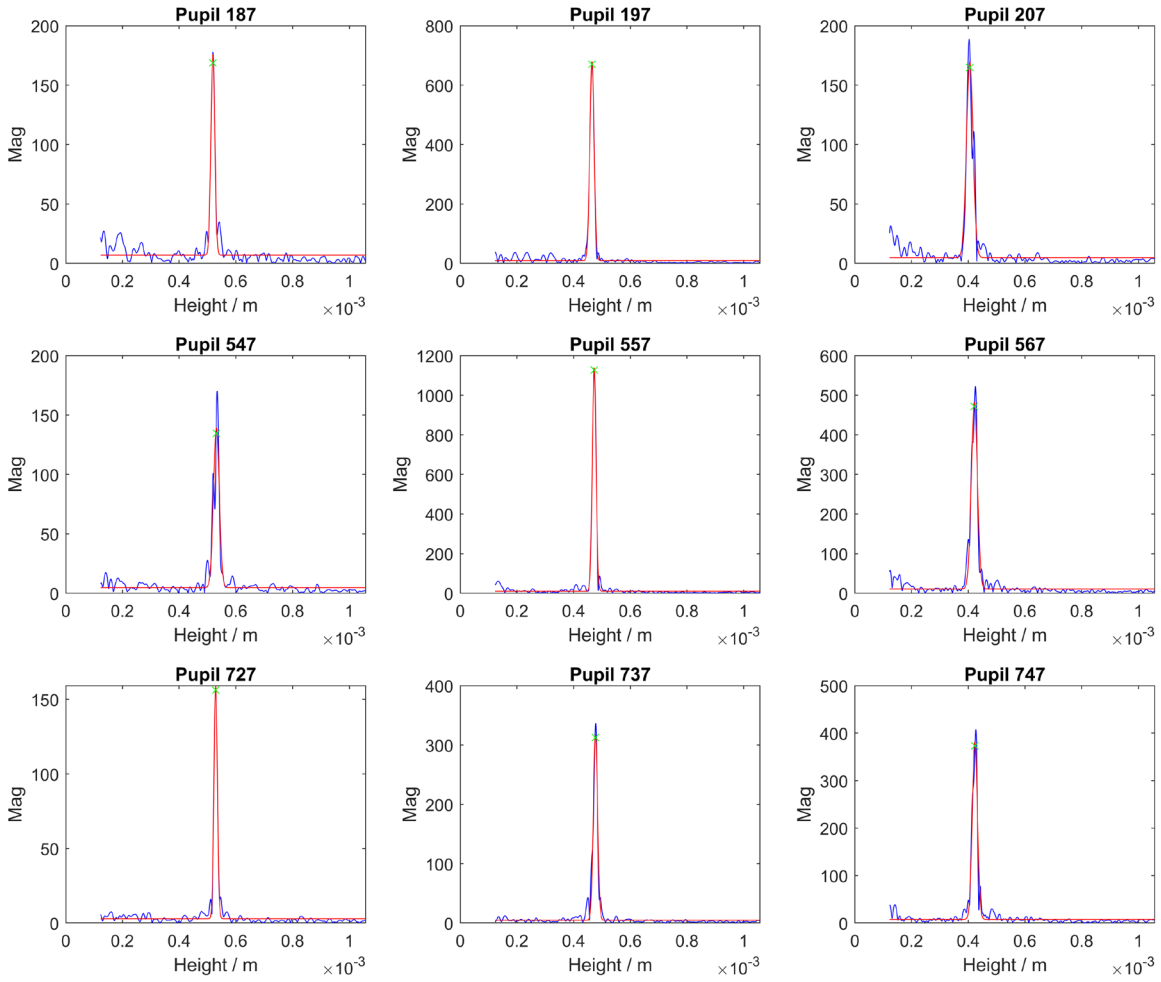

Figure 10. Blue: Magnitude of discrete Fourier transform (DFT) of 1D spectra from roughness gauge index N6 ($R_a = 0.8$ μm), with spectral envelope component removed, for nine representative channels. Red: 1D Gaussian fits to DFT.

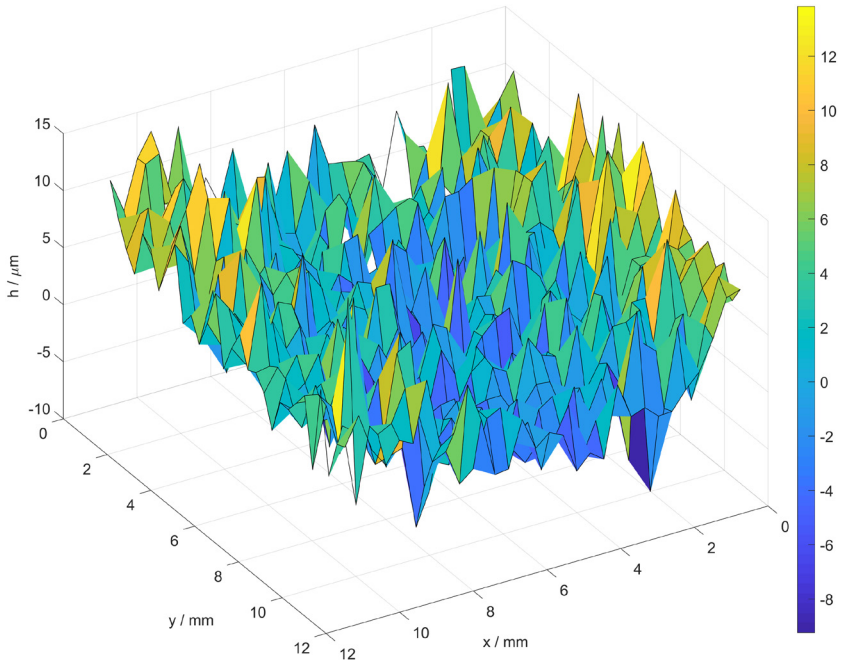

Figure 11. Reconstructed HSI surface height profile from 1D Gaussian peak position for roughness gauge index N6 ($R_a = 0.8$ μm).

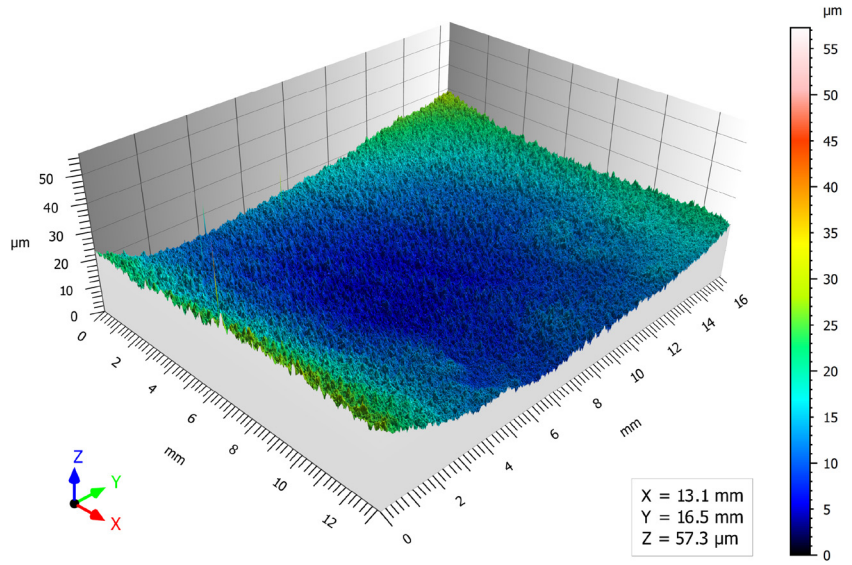

Figure 12. Control surface measurement of roughness gauge index N6 ($R_a = 0.8$ µm) on CSI with *XYZ* dimension legend.

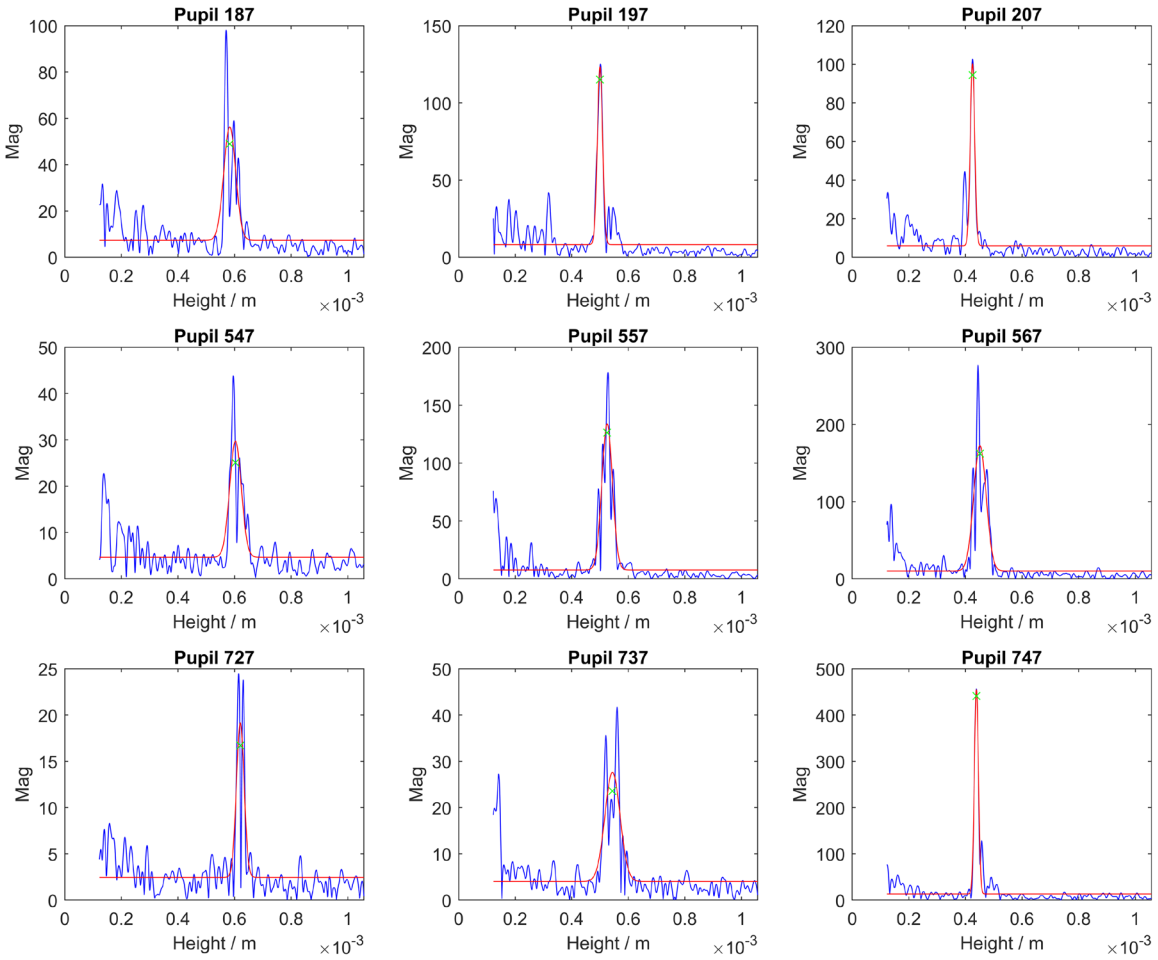

Figure 13. Blue: Magnitude of DFT of 1D spectra from roughness gauge index N10 ($R_a = 12.5$ µm) with spectral envelope component removed. Red: 1D Gaussian fit to DFT.

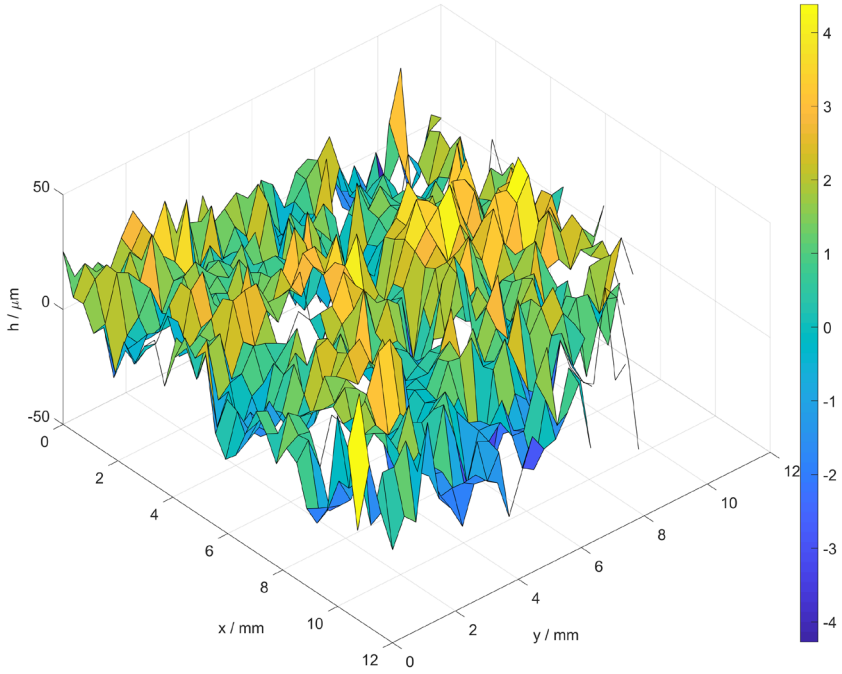

Figure 14. Reconstructed HSI surface height profile from 1D Gaussian peak position for roughness gauge index N10 ($R_a = 12.5$ um).

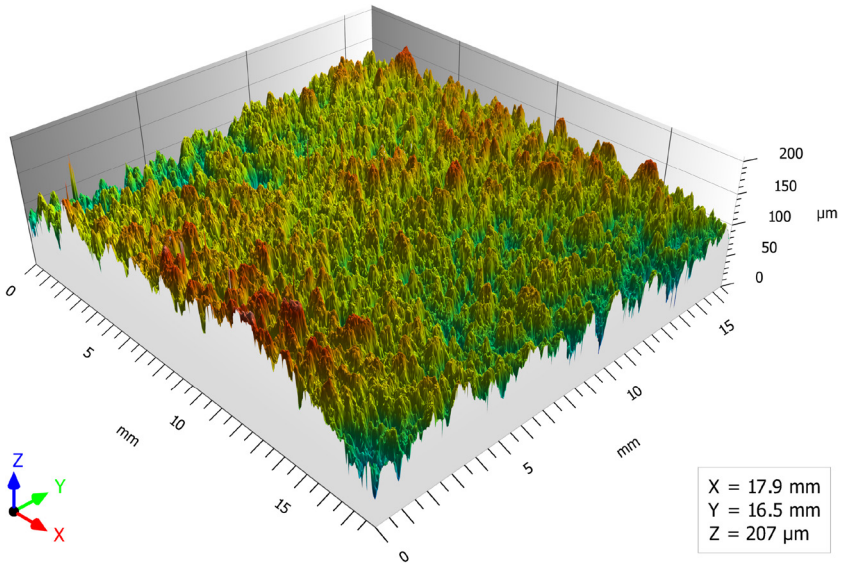

Figure 15. Control surface measurement of roughness gauge index N10 ($R_a = 12.5$ μm) on CSI with *XYZ* dimension legend.

$\overline{\sigma}_h$ and σ_{σ_h} values, and number of channels returning valid data, N_v, are given in table 3 and $\overline{\sigma}_h$ is plotted in figure 17 against the CSI-measured Sa. The vertical error bars here indicate the two sigma uncertainty in $\overline{\sigma}_h$, calculated as $U_{\overline{\sigma}_h} = 2\sigma_{\sigma_h}/\sqrt{N_v}$.

5. Discussion

The results from table 3 indicate generally good agreement between the CSI measurements and the nominal gauge R_a values. The exceptions are N7 and N8, where the CSI-measured S_a exceeded the nominal R_a value by up to 80%.

The S_a values from HSI are significantly higher than those from CSI at low roughness values (gauges N1–N6). This is because of the HSI noise floor: even with perfectly smooth samples, the standard deviation in height is ca. 0.5 μm [15]. Despite this, there is a gradual upward trend of the HSI measurements for the sub-μm roughness regime (figure 16, left curve). Very good agreement is apparent between the HSI S_a and CSI S_a values for the larger roughness value gauges corresponding to indices N7 to N11, where the HSI S_a value is mostly within a few per cent of (and at worst 24% away from) the CSI S_a. Although the N12 results are much less consistent, with a factor of about 2× between the CSI and

Table 3. Sample indices from N1–12, Nominal arithmetic roughness R_a as indicated for each roughness index; arithmetic mean surface roughness S_a as measured by CSI and HSI; mean and standard deviation of the Gaussian peak widths, $\overline{\sigma}_h$ and σ_{σ_h}, respectively; number of channels returning valid Fourier peaks, N_v; uncertainty in S_a resulting from an average of $\overline{\sigma}_h$ values over all N_v channels, U_{S_a}.

Sample	Nominal R_a/μm	CSI S_a/μm	HSI S_a/μm	HSI $\overline{\sigma}_h$/μm	HSI σ_{σ_h}/μm	HSI N_v	HSI U_{S_a}/μm
N1	0.025	0.0237	0.68	6.12	0.83	856	—
N2	0.05	0.0611	1.23	6.66	1.53	782	—
N3	0.1	0.1073	1.41	6.75	1.58	897	—
N4	0.2	0.2120	1.51	6.77	1.66	898	—
N5	0.4	0.4328	1.70	7.30	1.95	887	—
N6	0.8	0.647	2.35	8.25	2.46	873	0.19
N7	1.6	2.93	3.62	9.77	8.45	847	0.75
N8	3.2	4.38	4.49	11.2	8.80	830	0.90
N9	6.3	6.93	6.53	12.2	5.44	857	0.59
N10	12.5	13.5	13.6	17.8	9.71	849	1.3
N11	25.0	30.1	23.4	26.1	18.0	756	0.9
N12	50.0	51.8	102	93.8	116	53	8.8

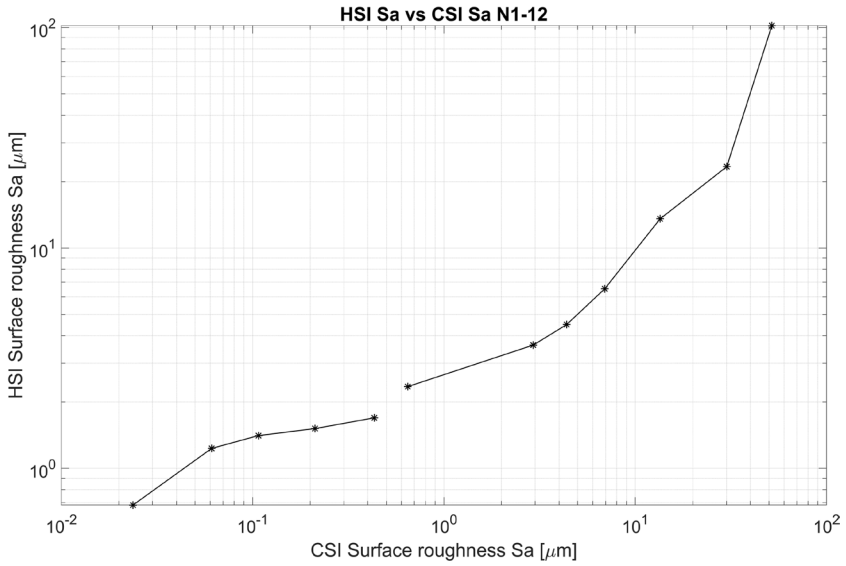

Figure 16. Surface arithmetic mean roughness S_a, as calculated from HSI-measured height fluctuations, for roughness gauge indices N1–12. The true surface roughness for each gauge was determined by CSI. Separate lines link the results from the ground and the cast gauges.

HSI readings, this is likely to be a consequence of the very low number of HSI channels with valid data ($N_v = 53$), due to the low light levels measured by the instrument for this particular gauge.

Turning to the Fourier peak width results, it is helpful first to understand the effect of roughness on the shape of the Fourier peaks, and on the spatial distribution of the scattered amplitude, by considering the following three imaging regimes:

(1) Lowest roughness values, with S_a in the range 0 to $\lambda/4$. This corresponds to the transition from smooth wavefronts to speckled wavefronts in the back-scattered light from the sample surface. The speckle pattern structure varies with wavelength, causing changes to the spectral envelope and hence gradual Fourier peak broadening as roughness increases.

(2) Intermediate roughness values, with S_a in the range $\lambda/4$ to l_c, where l_c is the coherence length of the light source (14 μm for the SLED source used here). The speckle pattern is fully developed, giving large fluctuations in object wave intensity from pinhole to pinhole, but the height fluctuations are not resolved in the axial direction.

(3) High roughness values, with S_a above l_c. Here the depth range of the scattering points that lie within the channel's footprint on the sample surface, is wide enough for some of the points to be resolved in the axial direction. The Fourier transform is analogous to the reconstruction of the scattering potential with a spectral optical coherence tomography system [21]. In such a case we can expect the width of the Fourier peak to be proportional to the depth range of the scattering points within the channel's footprint.

The Fourier peak width results in figure 17 show a gentle increase with CSI S_a in the sub-μm to μm roughness range (gauges N1–N8, regimes 1 and 2 above). Here the relevant floor is the peak width resulting from the finite bandwidth (ca.

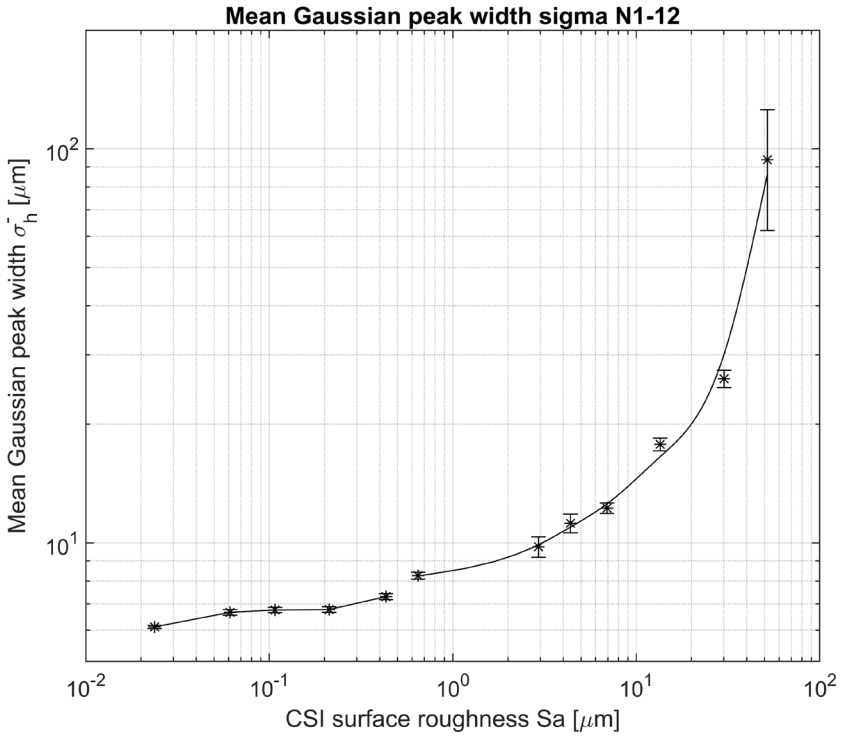

Figure 17. HSI peak width averaged over all valid channels, $\overline{\sigma}_h$, for roughness gauge indices N1–12. The true surface roughness for each gauge was determined by CSI. Separate lines link the results from the ground and the cast gauges.

50 nm) of the source. To quantify this in the limiting case of close-to-zero roughness, data from a sample consisting of a gold-coated mirror was processed through the same Gaussian-fitting described in the previous section. This yielded a mean peak width of 6.15 μm, with a standard deviation of 0.56 μm across all channels, which is very close to the N1 mean value of 6.12 μm.

Much stronger correlation between $\overline{\sigma}_h$ and CSI S_a is seen in the case of roughness values in the range 6 μm–50 μm (N9–N12, regime 3 above). The statistical significance of the changes in $\overline{\sigma}_h$ with S_a can be seen from the $U_{\overline{\sigma}_h}$ error bars. There is no overlap between bars for any of the gauges N6–N12, indicating that Fourier peak width has the potential to characterise surface roughness reliably for S_a values from 0.8 μm upwards, if data from several hundred channels can be averaged.

This may be quantified further by using the values for two sigma uncertainty in $\overline{\sigma}_h$ to estimate the corresponding uncertainty in S_a, denoted here U_{S_a}. The following equation models uncertainty propagation from $\overline{\sigma}_h$ to S_a:

$$U_{S_a} = U_{\overline{\sigma}_h} \Big/ \frac{\mathrm{d}f}{\mathrm{d}S_a} \tag{4}$$

where $f = f(S_a)$ is the expected mean Fourier peak width in the limit $N_v \to \infty$. The function $f(S_a)$ was estimated by least squares fitting (MATLAB Curve Fitting Toolbox, 'smoothing spline' fit function with roughness parameter = 0.994 819) to the N6–N12 data points, and is shown as the curve through those datapoints in figure 17. The resulting U_{S_a} values are tabulated in the final column of table 3; these characterise the deviations from the $f(S_a)$ curve due to the finite number of samples.

Data from a single pinhole suffers significant fluctuations, as indicated by the single-channel standard deviations shown in column 6 of table 3. This is a direct consequence of the sample microstructure and the size of the PSF: the design of the HSI system aims to optimise the lateral resolution by minimising the size of the PSF, however this limits the number of surface asperities contributing scattered light to each pinhole and hence causes significant statistical variations in peak width between channels. In effect, the local roughness value provided by each pinhole is *too* local to characterise the full surface reliably. One approach to address this could be to deliberately increase the PSF size, e.g. through defocus, so as to increase the number of scattering asperities contributing to each pinhole's signal. This would, however, be at the expense of the lateral resolution of the system, and hence would be likely to compromise the alternative method of roughness measurement based on direct calculation of S_a from the height maps.

6. Conclusion

A recently developed pinhole-array-based hyperspectral interferometer has been applied, for the first time, to measurements of optically rough surfaces. The instrument allows measurement of height over a 30 × 30 grid of sample points in a single shot, unlike traditional CSI, thus providing the potential for high speed characterisation of surface roughness. The HSI

S_a values for 12 different roughness gauges, covering the roughness range 0.025–50 μm, were compared with S_a values measured independently by CSI. Very good agreement was obtained for S_a values in the range 3–30 μm, where the HSI S_a values were mostly within a few per cent of (and at worst 24% away from) those measured by CSI S_a.

An alternative approach was also investigated that uses the peak width information from the Fourier transform of the 1D interference signals to estimate a local surface roughness value for each of the 900 channels. Large variations in peak width between channels is likely to be due to the small sampling region per pinhole, however when data from all channels are averaged, the peak width is shown to be a statistically reliable measure of local roughness in the intermediate to high roughness regime, i.e. for S_a values of 0.8 μm and above. The results from the study, together with the single-shot nature of HSI, demonstrate the technique's potential for real-time surface quality inspection in manufacturing.

Acknowledgments

The authors gratefully acknowledge useful discussions with David McKendrick and Nick Weston, Renishaw Plc, and financial support from Renishaw, the EPSRC Centre for Doctoral Training in Embedded Intelligence (EP/L014998/1), and the EPSRC Future Metrology Hub (EP/P006930/1).

Conflicts of interest

The authors declare no conflict of interest.

ORCID iDs

Tobias V Reichold https://orcid.org/0000-0002-9575-6139
Pablo D Ruiz https://orcid.org/0000-0003-3205-1665
Jonathan M Huntley https://orcid.org/0000-0003-3813-0401

References

[1] Reichold T V, Ruiz P D and Huntley J M Single-shot areal profilometry: towards real-time surface quality control in additive manufacturing *Int. Conf. of Manufacturing Research ICMR* (Skovde: IOS Press) (https://doi.org/10.3233/978-1-61499-902-7-101)
[2] Jared B H *et al* 2017 Additive manufacturing: toward holistic design *Scr. Mater.* **135** 141–7
[3] Triantaphyllou A *et al* 2015 Surface texture measurement for additive manufacturing *Surf. Topogr. Metrol. Prop.* **3** 1–8
[4] Thomas D S and Gilbert S W 2014 *Costs and Cost Effectiveness of Additive Manufacturing* (*Special Publication (NIST SP)*) (Gaithersburg, MD: National Institute of Standards and Technology) pp 5–47
[5] Norris G 2014 SpaceX Unveils 'Step Change' Dragon 'V2' (https://aviationweek.com/space/spacex-unveils-step-change-dragon-v2)
[6] SpaceX 2014 SpaceX Launches 3D-Printed Part to Space, Creates Printed Engine Chamber (www.spacex.com/news/2014/07/31/spacex-launches-3d-printed-part-space-creates-printed-engine-chamber-crewed)
[7] Kumbhar N and Mulay A 2016 Post processing methods used to improve surface finish of products which are manufactured by additive manufacturing technologies: a review vol 99 (https://doi.org/10.1007/s40032-016-0340-z)
[8] de Groot P 2011 Coherence scanning interferometry *Optical Measurement of Surface Topography* ed R Leach (Berlin: Springer) pp 187–208
[9] Danzl R, Helmli F and Scherer S 2009 Focus variation–a new technology for high resolution optical 3D surface metrology *The 10th Int. Conf. of the Slovenian Society for Non-Destructive Testing (Citeseer)*
[10] Newton L *et al* 2019 Areal topography measurement of metal additive surfaces using focus variation microscopy *Addit. Manuf.* **25** 365–89
[11] Gomez C *et al* 2017 Optimization of surface measurement for metal additive manufacturing using coherence scanning interferometry *Opt. Eng.* **56** 1–8
[12] Everton S K *et al* 2016 Review of *in situ* process monitoring and *in situ* metrology for metal additive manufacturing *Mater. Des.* **95** 431–45
[13] Marco G and Bianca Maria C 2017 Process defects and *in situ* monitoring methods in metal powder bed fusion: a review *Meas. Sci. Technol.* **28** 044005
[14] QISAB Products and solutions CWS 640. 20.3.2019 (http://qisab.com/products-solutions/products/cws640/)
[15] Ruiz P D and Huntley J M 2017 Single-shot areal profilometry using hyperspectral interferometry with a microlens array *Opt. Express* **25** 8801–15
[16] Huntley J M, Widjanarko T and Ruiz P D 2010 Hyperspectral interferometry for single-shot absolute measurement of two-dimensional optical path distributions *Meas. Sci. Technol.* **21** 075304
[17] Widjanarko T, Huntley J M and Ruiz P D 2012 Single-shot profilometry of rough surfaces using hyperspectral interferometry *Opt. Lett.* **37** 350–2
[18] Reichold T V, Ruiz P D and Huntley J M 2019 2500-channel single-shot areal profilometer using hyperspectral interferometry with a pinhole array *Opt. Lasers Eng.* **122** 37–48
[19] Reichold T V, Ruiz P D and Huntley J M 2018 Double-shot 3D displacement field measurement using hyperspectral interferometry *The 18th Int. Conf. on Experimental Mechanics, MPDI* p 518
[20] Bacon R *et al* 1995 3D spectrography at high spatial resolution. I. Concept and realization of the integral field spectrograph TIGER *Astron. Astrophys.* **113** 347
[21] Leitgeb R, Hitzenberger C K and Fercher A F 2003 Performance of fourier domain versus time domain optical coherence tomography *Opt. Express* **11** 889–94